Experimental Demonstration of Velocimetry by Actively Stabilized Coherent Optical Transfer

Benjamin P. Dix-Matthews,* David R. Gozzard, Skevos F.E. Karpathakis, Shane M. Walsh, Ayden McCann, Alex Frost, and Sascha W. Schediwy

International Centre for Radio Astronomy Research, Department of Physics, School of Physics, Mathematics, and Computing, The University of Western Australia, Perth, Western Australia 6009, Australia

(Received 17 January 2023; revised 30 March 2023; accepted 6 April 2023; published 4 May 2023)

We report on the development of a system called velocimetry by actively stabilized coherent optical transfer (VASCOT) that uses active optical phase tracking to measure the in-line velocity of retroreflecting targets with narrow-band photodetection. VASCOT is experimentally demonstrated over a 584-m atmospheric link to a corner-cube retroreflector (CCR) on an airborne drone. The in-line target-velocity measurement achieves residual uncertainties below 2 nm s^{-1} within 5 s of averaging. Cycle-slip-free phase tracking over the full 3-min experiment allows the relative target range to be tracked with a one-standard-deviation uncertainty of 39.5 nm. VASCOT also provides an absolute target-range measurement with a statistical error of ±13.7 mm, which agrees with an independent Global-Positioning-System- (GPS) derived range measurement to within the GPS uncertainty.

DOI: 10.1103/PhysRevApplied.19.054018

I. INTRODUCTION

Modern laser-based technologies offer unparalleled performance in position and velocity measurement. Laser ranging, or light detection and ranging (LiDAR), determines the absolute distance to a target by measuring the time of flight experienced by a reflected laser signal [1–5]. Laser ranging can be performed on both uncooperative targets, which are useful for navigation applications [6], and cooperative targets, which are useful for long-distance applications such as satellite [7–9] and lunar [10,11] laser ranging. Laser Doppler velocimetry uses the Doppler shift on a reflected laser signal to determine the in-line velocity, or range rate, of a target [2,12–15]. Typical laser Doppler velocimetry applications, including vibrometry [16], anemometry [17], and inertial navigation [3,18], focus on measurements over short (meter-scale) [3,18] or slow-moving [16,19] free-space links, often to noncooperative targets. Some applications, particularly related to satellite-orbit determination [20,21], require velocimetry over longer distances to cooperative targets.

Long-distance laser Doppler velocimetry offers some significant advantages but comes with correspondingly significant challenges. First, the Doppler shift is proportional to the carrier frequency and thus high laser frequencies result in large shifts. For example, a low-Earth-orbit satellite at an altitude of 500 km will produce Doppler shifts up to approximately ±10 GHz for a 1550-nm laser [20]. While this enables high-precision velocity measurements, it also introduces detection-bandwidth issues. Microwave photodetectors may have sufficient bandwidth to detect these frequency shifts but will suffer from signal-to-noise ratio problems. Second, the high directionality of laser-beam propagation enables efficient transmission over long distances but introduces pointing challenges. Atmospheric turbulence further complicates these pointing challenges, with active tracking of the target required to maintain the correct pointing.

We report on the development of a system called velocimetry by actively stabilized coherent optical transfer (VASCOT) that is capable of overcoming these challenges. VASCOT optically tracks the phase of a reflected signal to allow for narrow-band photodetection, thus transferring the detection-bandwidth requirements to the phase-tracking bandwidth. The pointing challenges are handled by an active tracking terminal capable of suppressing angular pointing errors to the moving target [22]. VASCOT is experimentally demonstrated over a 584-m atmospheric link to a corner-cube retroreflector (CCR) on an airborne drone, with cycle-slip-free phase tracking achieved for the 3-min experiment and a one-standard-deviation relative-range-measurement uncertainty of 39.5 nm. It is shown that the in-line target-velocity measurement can achieve residual uncertainties below 2 nm s^{-1} within 5 s of averaging. VASCOT is also able to provide an absolute-range measurement with a statistical error of ±13.7 mm, which agrees with an independent Global-Positioning-System- (GPS) derived range measurement to

*benjamin.dix-matthews@uwa.edu.au

 © 2023 American Physical Society

within the GPS uncertainty. In Sec. III D, atmospheric turbulence is shown to impose an additional noise floor on the physical accuracy of range and range-rate measurements.

II. METHODS

VASCOT is based on optical-metrology techniques initially developed for facilitating phase-stabilized coherent optical frequency transfer over atmospheric links [23–29]. These techniques rely on active phase locking to mitigate Doppler frequency shifts experienced during atmospheric propagation, thereby enabling high-resolution frequency measurements over long distances. VASCOT uses a similar system architecture but retroreflects the transmitted optical signal off the target and then uses the measured frequency and actuated frequency to precisely determine the Doppler shift experienced. The Doppler frequency shift is then used to calculate the in-line velocity (or range rate) of the target based on the speed of light.

The specific optical architecture used for VASCOT is shown in Fig. 1. While the primary focus of VASCOT is to accurately measure in-line target velocity, it is mathematically convenient to analyze the system in terms of range, or link-length, measurements.

VASCOT is designed to make two target-range measurements, partly as a byproduct of the active phase-tracking design and partly as a way of analyzing the measurement noise sources and verifying the measurement precision and accuracy. As described in Sec. III B, taking two range measurements also enables estimation of the absolute range. The primary range measurement, $r_1(t)$, is based on the time of flight experienced when the laser signal is initially retroreflected off the target. The laser signal received after this initial retroreflection is then frequency shifted by an acousto-optic modulator (AOM) and retransmitted off the target. The secondary range measurement, $r_2(t)$, is based on the time of flight experienced by this retransmitted signal. Detailed derivations of these range measurements are provided in Appendix A.

The resulting measurement equations are

$$r_1(t) \approx r_0 + \frac{c}{2n}\frac{\Delta\phi_{tr}(t) - \phi_{\text{meas}}(t)}{\omega_L + \omega_{tr}} - \frac{r_0}{2}\frac{\Delta\omega_{tr}(t) + \omega_{\text{meas}}(t)}{\omega_L + \omega_{tr}}, \tag{1}$$

and

$$r_2(t) \approx r_0 + \frac{c}{2n}\frac{\Delta\phi_{tr}(t) + \phi_{\text{meas}}(t)}{\omega_L + \omega_{tr} + 2\omega_{rc}} + \frac{r_0}{2}\frac{\Delta\omega_{tr}(t) - \omega_{\text{meas}}(t)}{\omega_L + \omega_{tr} + 2\omega_{rc}}, \tag{2}$$

where $\omega_L = 193.2$ THz is the seed-laser frequency, $\omega_{tr} = -85$ MHz is the nominal frequency of the top acousto-optic modulator (AOM), $\Delta\omega_{tr}(t)$ is the tunable frequency offset of the top AOM, $\Delta\phi_{tr}(t) = \int_0^t \Delta\omega_{tr}(t)dt$, $\omega_{rc} = +75$ MHz is the nominal frequency of the bottom AOM, c is the speed of light in a vacuum, n is the refractive index, $\phi_{\text{meas}}(t)$ is the initial optical phase measurement, and $\omega_{\text{meas}}(t) = d\phi_{\text{meas}}(t)/dt$. The accuracy of these range measurements is fundamentally limited by the knowledge of the refractive index, n, as is always the case when using time-of-flight measurements to determine distance [1,21,30]. For this demonstration, it is assumed that $n = 1$.

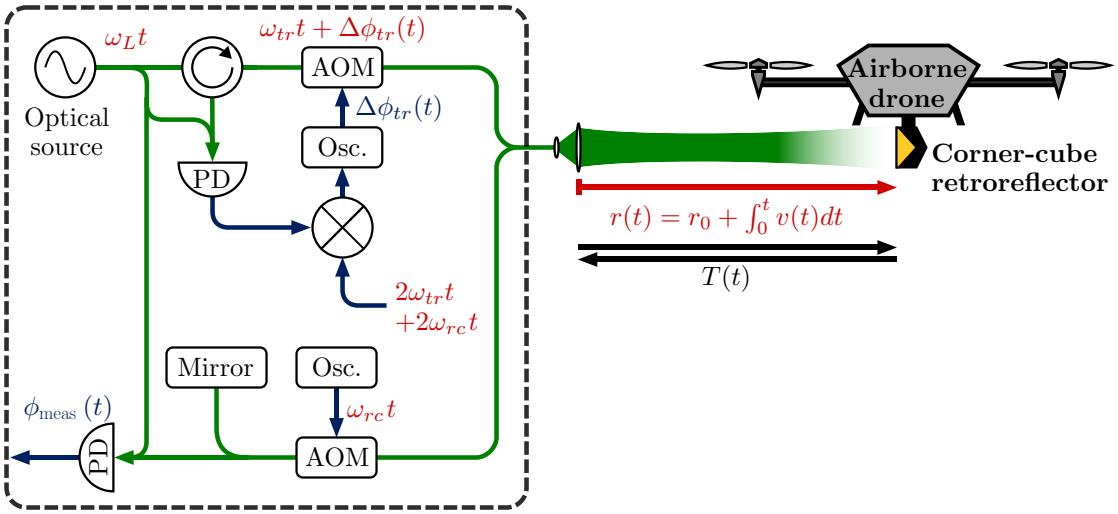

FIG. 1. A block diagram of the optical configuration used for VASCOT. The variables shown in blue text are the two specific phases measured by VASCOT. The green lines represent optical-frequency signals and the blue lines represent electrical signals. Abbreviations: AOM, acousto-optic modulator; Osc., electronic oscillator; PD, photodetector.

III. RESULTS

VASCOT is demonstrated over a free-space link to a Ø50.8 mm CCR on an airborne drone. The optical terminal is located at an altitude of 31 m above sea level and transmits an approximately −1.4-dBm (0.72-mW) optical beam with a $1/e^2$ radius and divergence of approximately 16.8 mm and 29 μrad, respectively. Using a GPS module with a nominal position accuracy of ±3.0 m [31], the starting altitude of the drone is measured to be 117 m above sea level and the initial separation between the drone and the optical terminal, r_0, is 584 m.

A continuous 3-min measurement of the drone position is made as the drone flies backward and forward at approximately 0.25 m s^{-1}. Figure 2 shows time series of the primary and secondary optically derived range and range-rate measurements. The difference between the primary and secondary measurements of the range [Fig. 2(c)] and the range rate [Fig. 2(f)] are shown in orange. After removing the linear drift by thermal calibration, as discussed in Sec. III A, the difference between the primary and secondary range measurements has a standard deviation of 39.5 nm. Position readings from the drone GPS are used to provide an independent course measurement of the range at 1-s intervals, shown as a black dashed line in Figs. 2(a)–2(c). The difference between the optically derived, $r(t)$, and GPS-derived, $r^{\mathrm{GPS}}(t)$, range measurements is shown in Fig. 3. The measurements show good agreement for the first 90 s and then, for the final 90 s, there is an approximately 2-m offset, which is still within the 3.0-m accuracy of the GPS used [31]. The macroscopic step in Fig. 3 of the GPS-derived range measurements suggests that the measured disagreement is dominated by GPS inaccuracy.

A. Thermal sensitivity

The difference between the range measurements obtained from the primary and secondary propagation, shown as orange in Fig. 2(c), exhibits an approximately linear drift over the measurement time that is likely caused by thermal drift, as the experiment is located in an outdoor environment and not actively temperature stabilized. Differential variations in the optical path length of non-common fiber will result in variations between the primary and secondary target-range measurements. Thermal drift causes fiber expansion and a change in refractive index, which lead to a change in the optical path length. Assuming an out-of-loop fiber length of L_0, a temperature variation of $\Delta T(t)$ will lead to a path-difference measurement of

$$\Delta L_{\leftrightarrow}(t) = n_{T_0}(\alpha + \eta)\Delta T(t) L_0, \tag{3}$$

where $n_{T_0} = 1.4515$ is the refractive index of silica, $\alpha = 0.55 \times 10^{-6}\ \mathrm{K}^{-1}$ is the coefficient of thermal expansion for single-mode fiber, and $\eta = 7 \times 10^{-6}\ \mathrm{K}^{-1}$ is the thermo-optic coefficient for single-mode fiber [32,33].

Thus, given a measurement of the thermally induced residual length difference, $d\Delta L_{\leftrightarrow}/dt$, the corresponding temperature gradient would be

$$\frac{d\Delta T(t)}{dt} = \frac{1}{n_{T_0}(\alpha + \eta) L_0} \frac{d\Delta L_{\leftrightarrow}}{dt}. \tag{4}$$

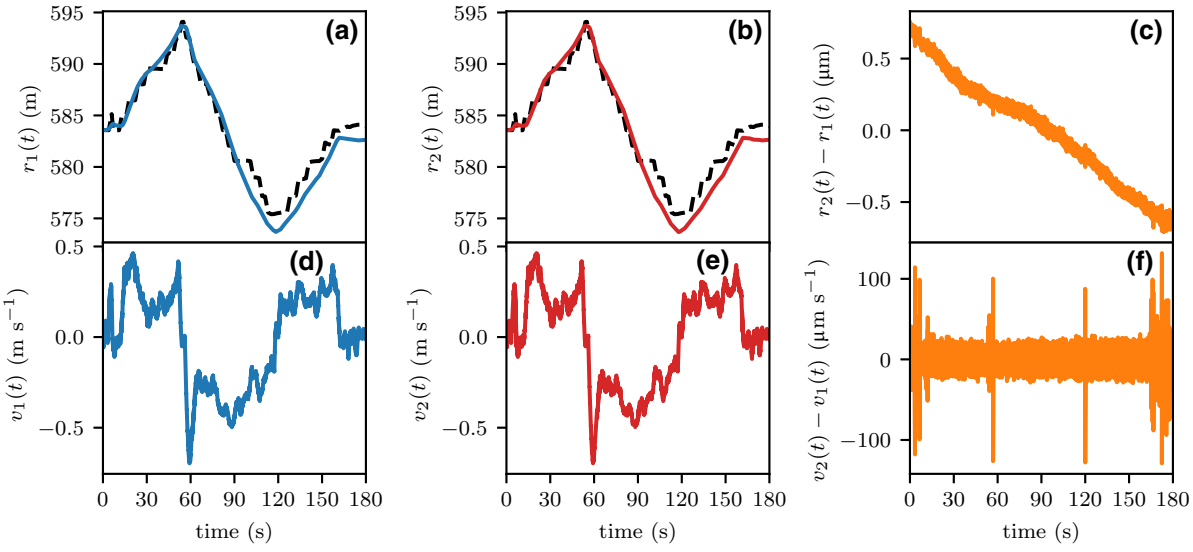

FIG. 2. Time-series results of the experimental demonstration to the airborne target at an initial separation of $r_0 = 584$ m: (a)–(c) target-range measurements; (d)–(f) in-line velocity measurements. Blue, measurements based on the primary time of flight; red, measurements based on the secondary time of flight; orange, the difference between equivalent primary and secondary measurements without the thermal calibration discussed in Sec. III A; black dashed, independent GPS-derived distance measurements.

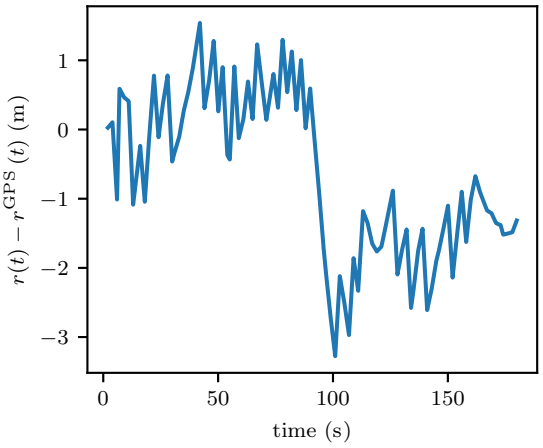

FIG. 3. The time-series difference between the optically and GPS-derived range measurements. The optically derived range measurement used, $r(t)$, is the primary measurement, $r_1(t)$. The GPS-derived range, $r^{\mathrm{GPS}}(t)$, is measured with a nominal accuracy of 3.0 m [31].

A linear fit of the measured residual path-length difference in Fig. 2(c) gives $r_T(t) = -7.14 \times 10^{-9}t + 6.45 \times 10^{-7}$; thus $d\Delta L_{\leftrightarrow}/dt \approx 7.14$ nm s^{-1}. The approximate length of noncommon fiber in the optical system is 2 m. Thus, Eq. (4) shows that the path-length change would correspond to a temperature gradient of $d\Delta T(t)/dt \approx 0.326$ mK s^{-1} or 1.17 K h^{-1}.

Figure 4 shows the air temperature in Perth on the day of the experiment. These data were obtained from the publicly available Integrated Surface Dataset (Global) maintained by the National Oceanic and Atmospheric Administration (NOAA) National Centers for Environmental Information [34]. The gray dashed line indicates when the experiment took place, at which time the temperature was 26.3 °C and the temperature gradient was 0.8 K h^{-1}. The red dashed line represents the predicted temperature gradient of 1.17 K h^{-1} that corresponds to the observed residual drift. The similarity of the predicted and measured temperature gradients indicates that thermal drift is the cause of the primary and secondary range-measurement drift. The approximately 0.4 K h^{-1} difference between the measured and predicted temperature gradients may be caused by a 2-h lag between the internal temperature of the fibers and the external environmental temperature.

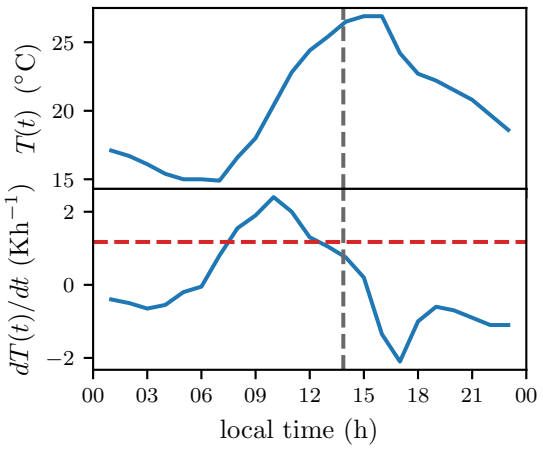

FIG. 4. The air temperature recorded in Perth on the day of the experiment. The gray dashed line indicates the time when the experiment took place. The red line shows the temperature gradient that would correspond to the residual drift between the range measurements obtained from the primary and secondary propagation. The figure has been prepared using data at Perth Airport from the NOAA National Centers for Environmental Information [34].

B. Optical estimate of initial range

As VASCOT takes two range measurements, each dependent on an initial target-range estimate, it is possible to estimate the initial target range directly from the optical phase measurements under the assumption that the primary and secondary propagation distances are equal: $(r_1(t) = r_2(t))$. After thermal calibration, as discussed in Sec. III A, this becomes $r_1(t) = r_2(t) - r_T(t)$, where $r_T(t) = -7.14 \times 10^{-9}t + 6.45 \times 10^{-7}$. Thus, by using Eqs. (1) and (2),

$$c\left[\frac{\Delta\phi_{tr}(t) - \phi_{\mathrm{meas}}(t)}{\omega_L + \omega_{tr}} - \frac{\Delta\phi_{tr}(t) + \phi_{\mathrm{meas}}(t)}{\omega_L + \omega_{tr} + 2\omega_{rc}}\right] + 2r_T(t) = r_0\left[\frac{\Delta\omega_{tr}(t) + \omega_{\mathrm{meas}}(t)}{\omega_L + \omega_{tr}} + \frac{\Delta\omega_{tr}(t) - \omega_{\mathrm{meas}}(t)}{\omega_L + \omega_{tr} + 2\omega_{rc}}\right]. \tag{5}$$

As is shown in Fig. 5, a linear fit of $f_\phi(t) = r_0 f_\omega(t)$ can be used to determine an estimate of the initial range, where $f_\phi(t) = c\,[(\Delta\phi_{tr}(t) - \phi_{\mathrm{meas}}(t))/(\omega_L + \omega_{tr}) - (\Delta\phi_{tr}(t) + \phi_{\mathrm{meas}}(t))/(\omega_L + \omega_{tr} + 2\omega_{rc})] + 2r_T(t)$ and $f_\omega(t) = [(\Delta\omega_{tr}(t) + \omega_{\mathrm{meas}}(t))/(\omega_L + \omega_{tr}) + (\Delta\omega_{tr}(t) - \omega_{\mathrm{meas}}(t))/(\omega_L + \omega_{tr} + 2\omega_{rc})]$. The blue trace shows the increased spread when the thermal-drift term in Eq. (5) is not considered. The red trace shows the improvement made after the thermal calibration. The orange trace shows the least-squares line of best fit, which corresponds to an initial link range of $r_0 = 581.5$ m. This fitted r_0 estimate has a one-standard-deviation statistical error of ±13.7 mm but has much higher systematic errors, largely due to uncertainty in the calibration procedure, which is discussed in Appendix B. The purple dashed line shows the equivalent model for the initial link-range estimate obtained from the GPS, $r_0 = 584$ m. There is a 2.5-m discrepancy between the initial range estimates obtained by the linear fit of Eq. (5) and the GPS, within the uncertainty of the GPS module. This suggests that VASCOT could effectively determine a valid estimate of the absolute target range. This would, however, require more accurate calibration of the time delays discussed in Appendix B.

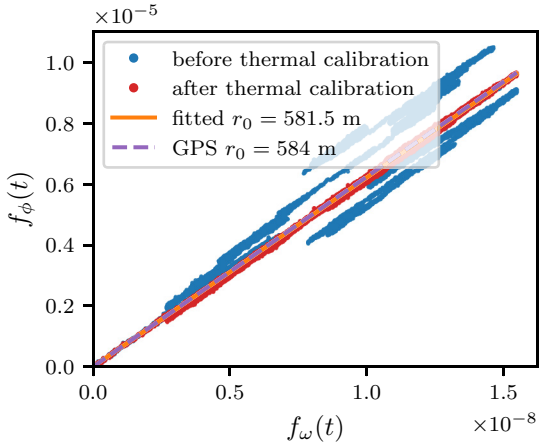

FIG. 5. Estimation of the initial range based on purely optical phase measurements. The scatter points are obtained from raw phase measurements (blue) and phase measurements after accounting for thermal drift (red). The orange line is a line of best fit, which corresponds to a target range of $r_0 = 581.5$ m and has a one-standard-deviation statistical error of ± 13.7 mm. The dashed purple line shows the modeled trend for the independently GPS-derived initial target range of $r_0 = 584$ m.

C. Velocity uncertainty results

The velocity uncertainty between the primary and secondary range-rate measurements, displayed in Fig. 2(f), is shown as a modified Allan deviation in Fig. 6. The orange trace is the uncertainty based on the optically derived estimate of the initial target range. The purple trace is the uncertainty assuming the initial target range derived from the independent GPS measurement.

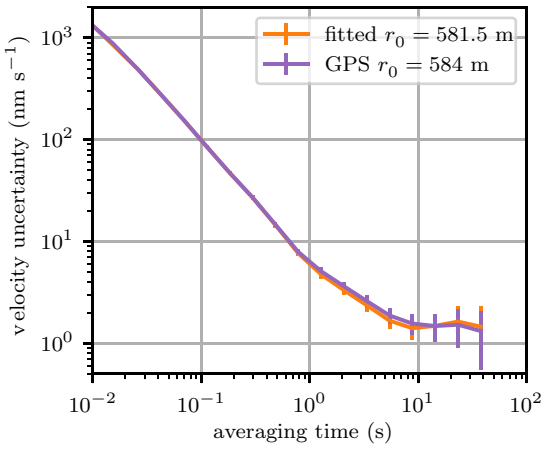

FIG. 6. The in-line velocity uncertainty expressed as a modified Allan deviation. The orange and purple lines, respectively, rely on the optically and GPS-derived initial target-range estimates. The error bars on each averaged velocity uncertainty, $\delta v(\tau)$, correspond to $\delta v(\tau)/\sqrt{N}$, where N is the number of velocity measurements taken at the averaging time τ.

The 2.5-m difference between the estimates of the initial target range does not lead to a significant change in the velocity-uncertainty characteristics. Both achieve velocity uncertainties below 2 nm s^{-1} within 5 s of averaging. Using the optically derived estimate for the initial range gives an optimum uncertainty of 1.4 nm s^{-1} after 9 s of averaging and the GPS-derived initial range gives an optimum uncertainty of 1.3 nm s^{-1} after 38 s of averaging.

D. Atmospheric turbulence analysis

Variations in refractive index caused by atmospheric turbulence will lead to time-of-flight fluctuations, thereby placing a fundamental accuracy limit on the target-range measurement made by VASCOT. For Kolmogorov turbulence under Taylor's theory of frozen turbulence, the predicted phase fluctuations will have a power spectral density of

$$S_\phi(f) = 0.016 k^2 C_n^2 L V^{5/3} f^{-8/3} \quad [\text{rad}^2\,\text{Hz}^{-1}], \tag{6}$$

where $k = 2\pi/\lambda$ is the wave number, C_n^2 is the turbulence structure constant, L is the free-space propagation distance, V is the wind speed, and f is the temporal frequency [35].

Atmospherically induced phase changes, $\delta\phi(t)$, will lead to variations in the measured target range according to $\delta r(t) = \frac{1}{2}\lambda/2\pi\,\delta\phi(t)$, where the $\frac{1}{2}$ factor accounts for the fact that the target range is determined from a retroreflected signal. Thus the expected atmospheric contribution to the range power spectral density is given by

$$S_r(f) = \left[\frac{\lambda}{4\pi}\right]^2 S_\phi(f) \quad [\text{m}^2\,\text{Hz}^{-1}]. \tag{7}$$

The atmospherically induced fluctuations in the measured target velocity will therefore have a power spectral density of

$$S_v(f) = 4\pi^2 f^2 S_r(f) \quad [\text{m}^2\,\text{s}^{-2}\,\text{Hz}^{-1}]. \tag{8}$$

An additional measurement was made by VASCOT over a 300-m link to a static CCR. This static measurement was taken approximately 2 h prior to the moving-drone measurement that is used in the rest of this paper. The average wind speed was approximately 6 m s^{-1} for both measurements.

Figure 7 shows the power spectral density of the measured target range and velocity for both the moving drone (blue) and the 300-m static target (red). Only the primary range measurement is shown, as the difference between primary and secondary is negligible in this context. The black dashed line provides the expected atmospheric contribution as modeled by Eq. (7), assuming a typical turbulence structure constant of $C_n^2 = 3 \times 10^{-14}$ m$^{-2/3}$, a link length of $L = 2 \times 300$ m, a wind speed of $V = 6$ m s^{-1}, and a wavelength of $\lambda = 1550$ nm.

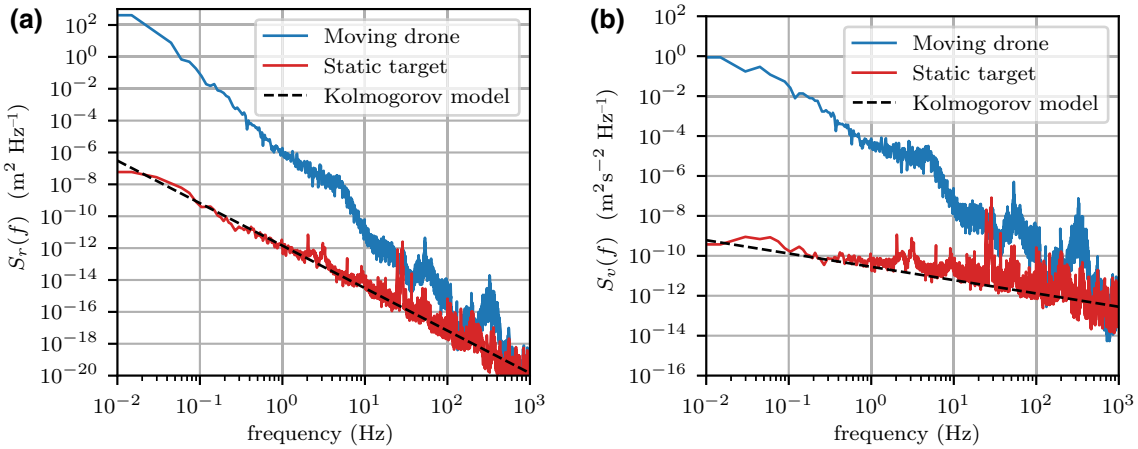

FIG. 7. The power spectral density of the measured target range (a) and velocity (b). Blue is for the moving drone and red is for the static 300-m target measurement. The black dashed line is the predicted contribution of atmospheric turbulence, calculated using Eqs. (7) and (8) assuming $C_n^2 = 3 \times 10^{-14}$ m$^{-2/3}$, $L = 2 \times 300$ m, $V = 6$ m s^{-1}, and $\lambda = 1550$ nm.

The static target measurement in red shows good agreement with the modeled atmospheric contribution, indicating that the measurement is dominated by turbulence. Therefore, Eqs. (7) and (8) provide a noise floor when using VASCOT terrestrially. The moving-drone measurement in blue is greater, especially < 10 Hz, indicating that physical drone movements and vibrations are dominant.

IV. DISCUSSION AND CONCLUSIONS

These results demonstrate the efficacy of VASCOT at precisely measuring the in-line velocity of a cooperative airborne target. VASCOT uses active phase locking to continuously track the target range to submicrometer precision over the full 3-min measurement window. The optically and GPS-derived target-range measurements show good agreement. After the thermal calibration, in Sec. III A, VASCOT is able to estimate the absolute target range based purely on the optical phase measurements. The optically derived initial target-range estimate of $r_0 = 581.5$ m, with a standard deviation of ± 13.7 mm, agrees well with the equivalent GPS range measurement of $r_0 = 584$ m. VASCOT is able to achieve in-line velocity uncertainties below 2 nm s^{-1} within 5 s of averaging using either initial target-range estimate. Unfortunately, as discussed in Sec. III D, atmospheric turbulence will impose an additional noise floor onto the practical range and range-rate measurements achievable. This occurs because VASCOT measures optical path length, as opposed to physical range. The range and velocity measurements are, therefore, limited by knowledge of the propagation-medium refractive index. Equations (7) and (8) give the noise floor imposed by atmospheric turbulence on VASCOT. In a different propagation media, such as a vacuum, this imposed noise floor will change or disappear.

The impressive velocimetry performance achieved by VASCOT is due to the high-precision optical phase measurements enabled by active phase locking. However, phase locking introduces challenges related to initial target acquisition and servo actuation range. In this demonstration, the airborne target is approximately static during the initial phase locking to ensure that the unknown initial Doppler shift is low and the system can be locked without difficulty. Acquiring a moving target is more complicated. Initial target acquisition requires that the returned Doppler signal has sufficient signal-to-noise ratio and is within the detection bandwidth of the phase-locking system. Unfortunately, a wide detection bandwidth will degrade the signal-to-noise ratio [21]. The transmitted optical signal could be swept in frequency to bring the returned frequency within the detection bandwidth before phase locking, enabling a wide detection range with a low detection bandwidth at the expense of increased search time. Additionally, *a priori* knowledge of the target velocity could be used to narrow the spectral search window. An applicable case is satellite orbitography, where velocity estimates can be accurate to better than 1 cm s^{-1} [21]. For airborne targets, the uncertainty in initial velocity estimates may be higher, necessitating a wider spectral search window. However, a lower transmission range will allow for greater reflected power, thereby enabling wider detection bandwidths to be employed. The exact balance between the detection bandwidth, the spectral search window, and the signal-to-noise ratio will depend on the specific application of VASCOT.

Once locked, the actuation bandwidth of the stabilization system will then set an upper limit on the measurable target velocity. The achievable actuation bandwidth in this demonstration is ± 1 MHz, set by the tuning range of the transmission AOM, $\Delta\omega_{tr}(t)$, thereby limiting the in-line target velocity to < 0.77 m s^{-1}. To increase the measurable target velocity, VASCOT would need to be redesigned

with a wider tuning range. To track a low-Earth-orbit satellite at an altitude of 500 m, a tuning range of ±10 GHz is required [20]. A system based on thermally tuning a laser, as has been developed in Ref. [21], could achieve the required tuning range.

ACKNOWLEDGMENTS

We would like to thank Peter Wolf for his assistance with the noise analysis. This work has been supported by the SmartSat CRC, whose activities are funded by the Australian Government's CRC Program. D.R.G. is supported by a Forrest Research Foundation Fellowship. S.F.E.K. is supported by a SmartSat CRC Ph.D. Scholarship.

APPENDIX A: RANGE-MEASUREMENT DERIVATION

Expressions for the primary time of flight and the secondary time of flight are derived in Appendixes A 1 and A 2. In Appendix A 3, expressions for the corresponding link-length measurements are derived based on consideration of the free-space link architecture. The final range measurements given in Eqs. (A13) and (A14) are then derived in Appendix A 4. The system calibrations required are discussed in Appendix B.

1. Primary time-of-flight measurement

In our demonstration, the primary optical carrier is produced by a seed laser of frequency $\omega_L = 193.2$ THz. During transmission, this optical signal is frequency shifted by $\omega_{tr} + \Delta\omega_{tr}(t)$ using an AOM, where $\omega_{tr} = -85$ MHz is the nominal frequency of the AOM and $\Delta\omega_{tr}(t)$ is a tunable offset. This tunable offset changes the phase of the outgoing signal by $\Delta\phi_{tr}(t) = \int_0^t \Delta\omega_{tr}(t)dt$. This tunable offset is used in a servo loop to precompensate for the frequency shifts experienced over the free-space link.

The transmitted optical beam propagates a distance of $r(t)$ to the airborne target, where it is reflected by a corner-cube retroreflector (CCR). The phase of this returned optical signal is time delayed by the net optical time of flight, $T_1(t)$. This reflected time-delayed signal is then frequency shifted by $\omega_{rc} = +75$ MHz using an AOM and the phase is measured by optically beating the signal against the seed laser of frequency ω_L and then electrically down-converting by a frequency of $\omega_{tr} + \omega_{rc}$, resulting in

$$\begin{aligned}\phi_{\text{meas}}(t) = {} & [t - T_1(t)](\omega_L + \omega_{tr}) + \Delta\phi_{tr}(t - T_1(t)) \\ & + t\omega_{rc} - t(\omega_{rc} + \omega_L + \omega_{tr}) + \phi_1^0. \end{aligned} \tag{A1}$$

The static phase term ϕ_1^0 accounts for the fact that this is a relative phase measurement and only measures deviation from some initial phase.

Thus, the optical primary time of flight is measured as

$$T_1(t) = \frac{\Delta\phi_{tr}(t - T_1(t)) - \phi_{\text{meas}}(t) + \phi_1^0}{\omega_L + \omega_{tr}}. \tag{A2}$$

2. Secondary time-of-flight measurement

A second measurement of the optical time of flight is made by frequency shifting a portion of the received optical signal by ω_{rc} and then retransmitting it back over the atmospheric link via the retroreflecting target. The phase of the signal launched back over the link is given by

$$\phi_{\text{return}}(t) = t(\omega_L + \omega_{tr} + 2\omega_{rc}) + \phi_{\text{meas}}(t). \tag{A3}$$

After passing back over the free-space link and through the transmission AOM, this optical signal is mixed down optically and then electrically to form an error signal of

$$\begin{aligned}\phi_{\text{err}}(t) = {} & [t - T_2(t)]\,(\omega_L + \omega_{tr} + 2\omega_{rc}) \\ & + \phi_{\text{meas}}(t - T_2(t)) \\ & + \omega_{tr}t + \Delta\phi_{tr}(t) \\ & - t(2\omega_{rc} + \omega_L + 2\omega_{tr}) + \phi_2^0, \end{aligned} \tag{A4}$$

where ϕ_2^0 accounts for this being a relative phase measurement.

The transmission AOM is driven by a control loop to ensure that this error signal is suppressed ($\phi_{\text{err}}(t) = 0$). Thus,

$$\begin{aligned} 0 = {} & -T_2(t)[\omega_L + \omega_{tr} + 2\omega_{rc}] \\ & + \Delta\phi_{tr}(t) + \phi_{\text{meas}}(t - T_2(t)) + \phi_2^0. \end{aligned} \tag{A5}$$

The secondary time of flight is therefore measured as

$$T_2(t) = \frac{\Delta\phi_{tr}(t) + \phi_{\text{meas}}(t - T_2(t)) + \phi_2^0}{\omega_L + \omega_{tr} + 2\omega_{rc}}. \tag{A6}$$

3. Free-space link description

The optical time of flight, $T(t)$, in terms of the distance between the transmitter and the retroreflecting target, $r(t)$, is

$$T(t) = 2\frac{n}{c}\left[r\left(t - \frac{T(t)}{2}\right)\right], \tag{A7}$$

where c is the speed of light in a vacuum and n is the refractive index of the propagation medium.

Thus the primary, $T_1(t)$, and secondary, $T_2(t)$, optical time-of-flight measurements can be used to obtain two

measurements of the distance between the transmitter and the retroreflecting target,

$$r_1(t) = \frac{c}{2n} T_1\left(t + \frac{T_1(t)}{2}\right) = \frac{c}{2n} \frac{\Delta\phi_{tr}\left(t - \frac{T_1(t)}{2}\right) - \phi_{\text{meas}}\left(t + \frac{T_1(t)}{2}\right) + \phi_1^0}{\omega_L + \omega_{tr}} \tag{A8}$$

and

$$r_2(t) = \frac{c}{2n} T_2\left(t + \frac{T_2(t)}{2}\right) = \frac{c}{2n} \frac{\Delta\phi_{tr}\left(t + \frac{T_2(t)}{2}\right) + \phi_{\text{meas}}\left(t - \frac{T_2(t)}{2}\right) + \phi_2^0}{\omega_L + \omega_{tr} + 2\omega_{rc}}. \tag{A9}$$

4. Linear approximations

These expressions can be approximated to allow for the calculation of the target range based on the optical phase measurements $\phi_{\text{meas}}(t)$ and $\Delta\omega_{tr}(t)$. Taking a first-order Taylor expansion of the time-delayed terms yields

$$r_1(t) \approx \frac{c}{2n} \frac{\Delta\phi_{tr}(t) - \phi_{\text{meas}}(t) + \phi_1^0}{\omega_L + \omega_{tr}} - \frac{cT_1(t)}{4n} \frac{\Delta\omega_{tr}(t) + \omega_{\text{meas}}(t)}{\omega_L + \omega_{tr}} \tag{A10}$$

and

$$r_2(t) \approx \frac{c}{2n} \frac{\Delta\phi_{tr}(t) + \phi_{\text{meas}}(t) + \phi_2^0}{\omega_L + \omega_{tr} + 2\omega_{rc}} + \frac{cT_2(t)}{4n} \frac{\Delta\omega_{tr}(t) - \omega_{\text{meas}}(t)}{\omega_L + \omega_{tr} + 2\omega_{rc}}, \tag{A11}$$

where $\omega_{\text{meas}}(t) = d\phi_{\text{meas}}(t)/dt$ and $\Delta\omega_{tr}(t) = d\Delta\phi_{tr}(t)/dt$.

Next, the initial time of flight is approximated as

$$\begin{cases} T_1^0 \approx \frac{c\phi_1^0}{2n(\omega_L+\omega_{tr})} \approx \frac{2r_0 n}{c}, \\ T_2^0 \approx \frac{c\phi_2^0}{2n(\omega_L+\omega_{tr}+2\omega_{rc})} \approx \frac{2r_0 n}{c}, \end{cases} \tag{A12}$$

where r_0 is an estimate of the initial link length.

Finally, we approximate the remaining time-of-flight terms $T_1(t)$ and $T_2(t)$ as T_1^0 and T_2^0. This approximation relies on the assumption that the initial link length is significantly greater than any deviations during the measurement.

Thus, the resulting measurement equations are

$$r_1(t) \approx r_0 + \frac{c}{2n} \frac{\Delta\phi_{tr}(t) - \phi_{\text{meas}}(t)}{\omega_L + \omega_{tr}} - \frac{r_0}{2} \frac{\Delta\omega_{tr}(t) + \omega_{\text{meas}}(t)}{\omega_L + \omega_{tr}} \tag{A13}$$

and

$$r_2(t) \approx r_0 + \frac{c}{2n} \frac{\Delta\phi_{tr}(t) + \phi_{\text{meas}}(t)}{\omega_L + \omega_{tr} + 2\omega_{rc}} + \frac{r_0}{2} \frac{\Delta\omega_{tr}(t) - \omega_{\text{meas}}(t)}{\omega_L + \omega_{tr} + 2\omega_{rc}}. \tag{A14}$$

APPENDIX B: MEASUREMENT CALIBRATION

Independent optically and GPS-derived target-range measurements are taken in this experiment. In order to compare these measurements, they must each be referenced to a common datum. In this work, the target range is defined as the separation between the exit aperture of the optical transmission terminal and the CCR. All range measurements must take this definition into account.

The GPS-derived range measurements agree with this target-range definition to within the uncertainty of the GPS measurement. The optically derived range measurement requires additional calibration to remove the time-of-flight contributions made by the static optical fiber in the system and leading to the exit aperture of the transmission terminal.

1. GPS-derived range measurement

The GPS range measurement is based on the separation of two measured locations. The first is the longitude, latitude, and elevation measured by a stationary GPS module placed within 10 cm of the exit aperture and averaged over the entire measurement. As the optical terminal turns to track the airborne drone, the location of the exit aperture will change by a negligible amount compared to the uncertainty of the GPS module. The second is the longitude, latitude, and elevation measured by the GPS module on the airborne drone, located next to the CCR to within 5 cm. As the nominal position accuracy of the GPS is ± 3.0 m [31], this uncertainty will dominate the GPS-derived range measurement and thus no further measurement calibration is necessary.

2. Time-of-flight contributions by optical fiber

Figure 8 details the fiber lengths that contribute to the time-of-flight measurements made by VASCOT. The lengths of these fibers must be taken into account when calibrating the system, so that the measured target-range distances correspond to the distance from the exit aperture as discussed in Appendix B. To understand which fibers

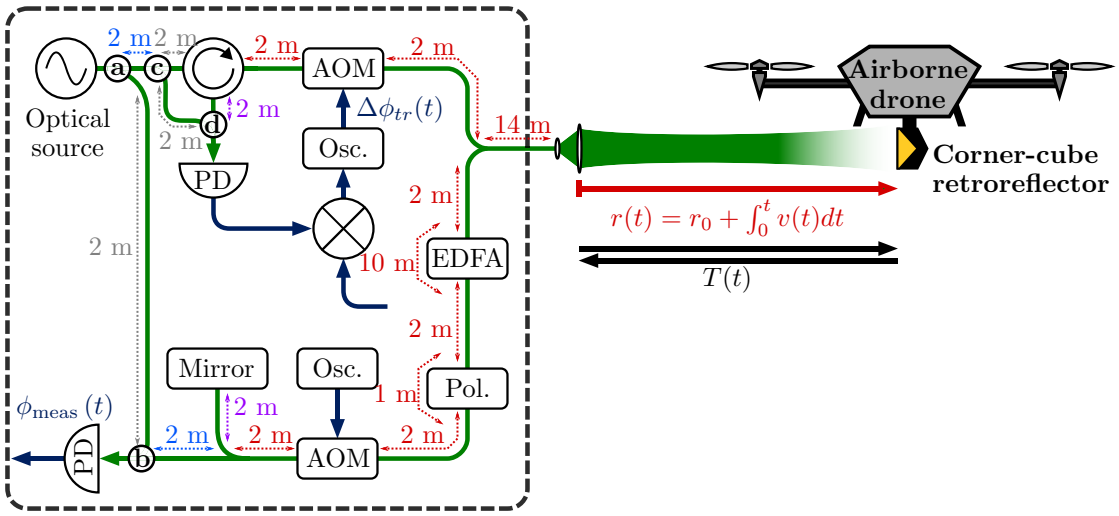

FIG. 8. A block diagram of the optical configuration used for VASCOT, with details of the lengths of fibers contributing to the time-of-flight measurements. The variables shown in blue text are the two specific phases measured by VASCOT. The green lines represent optical-frequency signals and the blue lines represent electrical signals. The red text contributes to both the primary and secondary time-of-flight measurements. The purple text contributes to only the primary time-of-flight measurement. The light-blue text contributes to only the secondary time-of-flight measurement. The gray text does not contribute to either time-of-flight measurement. Splitters **a** and **b** indicate the ends of the Mach-Zehnder interferometer corresponding to the primary time-of-flight measurement. Splitters **c** and **d** indicate the ends of the Mach-Zehnder interferometer corresponding to the secondary time-of-flight measurement. Abbreviations: AOM, acousto-optic modulator; EDFA, bidirectional erbium-doped fiber amplifier; Osc., electronic oscillator; PD, photodetector, Pol., polarization controller.

contribute to either the primary or secondary time-of-flight measurements, it is important to identify the interferometers making each of the measurements. The primary time of flight is measured by the Mach-Zehnder interferometer formed by splitters **a** and **b** in Fig. 8. The secondary time of flight is measured by the Mach-Zehnder interferometer formed by splitters **c** and **d** in Fig. 8. Each interferometer effectively compares the length of a short arm against a long arm that passes over the atmospheric link, with the difference corresponding to the target-range measurement. Gray text indicates fiber lengths that do not contribute to either time-of-flight measurement, as they are common between both arms of each interferometer. Red text indicates the fiber lengths that contribute to both the primary and secondary time-of-flight measurements. The purple text corresponds to fiber lengths that only contribute to the primary time-of-flight measurement. The light-blue text indicates fiber lengths that only contribute to the secondary time-of-flight measurement. Thus, the net fiber lengths contributing to the primary and secondary time-of-flight measurements are both approximately 55 m. All fiber is SMF-28 optical fiber, with a refractive index of $n = 1.467$. This contribution can be calibrated out of the range measurement by letting $r_0^{\mathrm{corrected}} = r_0 - 55 \times 1.467/2$. The factor of 2 accounts for the fact that the target range corresponds to half the time of flight, as discussed in Sec. A 3.

By making this calibration, the GPS-derived and the optically derived range measurements can then be directly compared. This calibration is made in all data presented in this paper. In future experiments, this calibration could be done with greater accuracy by directly measuring the additional time-of-flight contributions over a well-characterized static link.

[1] E. D. Caldwell, L. C. Sinclair, N. R. Newbury, and J.-D. Deschenes, The time-programmable frequency comb and its use in quantum-limited ranging, Nature **610**, 667 (2022).
[2] M. M. Bayer and O. Boyraz, Ranging and velocimetry measurements by phase-based MTCW lidar, Opt. Express **29**, 13552 (2021).
[3] J. Zhou, X. Nie, and J. Lin, A novel laser Doppler velocimeter and its integrated navigation system with strapdown inertial navigation, Opt. Laser Technol. **64**, 319 (2014).
[4] J. T. Spollard, L. E. Roberts, C. S. Sambridge, K. McKenzie, and D. A. Shaddock, Mitigation of phase noise and Doppler-induced frequency offsets in coherent random amplitude modulated continuous-wave LiDAR, Opt. Express **29**, 9060 (2021).
[5] D. R. Gozzard, L. E. Roberts, J. T. Spollard, P. G. Sibley, and D. A. Shaddock, Fast beam steering with an optical phased array, Opt. Lett. **45**, 3793 (2020).
[6] Y. Li and J. Ibanez-Guzman, Lidar for autonomous driving: The principles, challenges, and trends for automotive lidar

and perception systems, IEEE Signal Process. Mag. **37**, 50 (2020).

[7] J. J. Degnan, Millimeter accuracy satellite laser ranging: A review, Contrib. Space Geod. Geodyn.: Technol. **25**, 133 (1993).

[8] M. Wilkinson, U. Schreiber, I. Procházka, C. Moore, J. Degnan, G. Kirchner, Z. Zhongping, P. Dunn, V. Shargorodskiy, and M. Sadovnikov, *et al.*, The next generation of satellite laser ranging systems, J. Geod. **93**, 2227 (2019).

[9] K. Sośnica, D. Thaller, R. Dach, P. Steigenberger, G. Beutler, D. Arnold, and A. Jäggi, Satellite laser ranging to GPS and GLONASS, J. Geod. **89**, 725 (2015).

[10] J. Müller, T. W. Murphy, U. Schreiber, P. J. Shelus, J.-M. Torre, J. G. Williams, D. H. Boggs, S. Bouquillon, A. Bourgoin, and F. Hofmann, Lunar Laser Ranging: A tool for general relativity, lunar geophysics and Earth science, J. Geod. **93**, 2195 (2019).

[11] J. Chabé, C. Courde, J.-M. Torre, S. Bouquillon, A. Bourgoin, M. Aimar, D. Albanese, B. Chauvineau, H. Mariey, and G. Martinot-Lagarde, *et al.*, Recent progress in lunar laser ranging at Grasse laser ranging station, Earth Space Sci. **7**, e2019EA000785 (2020).

[12] R. G. Frehlich and M. J. Kavaya, Coherent laser radar performance for general atmospheric refractive turbulence, Appl. Opt. **30**, 5325 (1991).

[13] Y. Li, E. Dieussaert, and R. Baets, Miniaturization of laser Doppler vibrometers—a review, Sensors **22**, 4735 (2022).

[14] C. J. Karlsson, F. A. Olsson, D. Letalick, and M. Harris, All-fiber multifunction continuous-wave coherent laser radar at 1.55 μm for range, speed, vibration, and wind measurements, Appl. Opt. **39**, 3716 (2000).

[15] S. Wolfe, T. Shirahata, S. Yamashita, and S. Y. Set, in *Conference on Lasers and Electro-Optics* (Optica Publishing Group, 2022), p. ATu4M.7.

[16] P. Gueguen, V. Jolivet, C. Michel, and A.-S. Schveitzer, Comparison of velocimeter and coherent lidar measurements for building frequency assessment, Bull. Earthquake Eng. **8**, 327 (2010).

[17] F. Durst, A. Melling, and J. H. Whitelaw, *Principles and Practice of laser-Doppler Anemometry* Vol. 76 (Academic Press, New York, 1976), 47019.

[18] Q. Fu, Y. Liu, Z. Liu, S. Li, and B. Guan, High-accuracy SINS/LDV integration for long-distance land navigation, IEEE ASME Trans. Mechatron. **23**, 2952 (2018).

[19] H. W. Mocker and P. E. Bjork, High accuracy laser Doppler velocimeter using stable long-wavelength semiconductor lasers, Appl. Opt. **28**, 4914 (1989).

[20] B. P. Dix-Matthews, S. W. Schediwy, D. R. Gozzard, S. Driver, K. U. Schreiber, R. Carman, and M. Tobar, Methods for coherent optical Doppler orbitography, J. Geod. **94**, 1 (2020).

[21] N. Chiodo, K. Djerroud, O. Acef, A. Clairon, and P. Wolf, Lasers for coherent optical satellite links with large dynamics, Appl. Opt. **52**, 7342 (2013).

[22] S. M. Walsh, S. F. E. Karpathakis, A. S. McCann, B. P. Dix-Matthews, A. M. Frost, D. R. Gozzard, C. T. Gravestock, and S. W. Schediwy, Demonstration of 100 Gbps coherent free-space optical communications at LEO tracking rates, Sci. Rep. **12**, 1 (2022).

[23] B. P. Dix-Matthews, S. W. Schediwy, D. R. Gozzard, E. Savalle, F.-X. Esnault, T. Lévèque, C. Gravestock, D. D'Mello, S. Karpathakis, M. Tobar, and P. Wolf, Point-to-point stabilized optical frequency transfer with active optics, Nat. Commun. **12**, 515 (2021).

[24] D. R. Gozzard, S. W. Schediwy, B. Stone, M. Messineo, and M. Tobar, Stabilized Free-Space Optical Frequency Transfer, Phys. Rev. Appl. **10**, 024046 (2018).

[25] D. R. Gozzard, L. A. Howard, B. P. Dix-Matthews, S. F. E. Karpathakis, C. T. Gravestock, and S. W. Schediwy, Ultrastable Free-Space Laser Links for a Global Network of Optical Atomic Clocks, Phys. Rev. Lett. **128**, 020801 (2022).

[26] H. J. Kang, J. Yang, B. J. Chun, H. Jang, B. S. Kim, Y.-J. Kim, and S.-W. Kim, Free-space transfer of comb-rooted optical frequencies over an 18 km open-air link, Nat. Commun. **10**, 1 (2019).

[27] S. Chen, F. Sun, Q. Bai, D. Chen, Q. Chen, and D. Hou, Sub-picosecond timing fluctuation suppression in laser-based atmospheric transfer of microwave signal using electronic phase compensation, Opt. Commun. **401**, 18 (2017).

[28] K. Djerroud, O. Acef, A. Clairon, P. Lemonde, C. N. Man, E. Samain, and P. Wolf, Coherent optical link through the turbulent atmosphere, Opt. Lett. **35**, 1479 (2010).

[29] B. P. Dix-Matthews, D. R. Gozzard, S. F. E. Karpathakis, C. T. Gravestock, and S. W. Schediwy, Ultra-wideband free-space optical phase stabilization, IEEE Commun. Lett., 1 (2021),.

[30] B. K. Stuhl, Atmospheric refraction corrections in ground-to-satellite optical time transfer, Opt. Express **29**, 13706 (2021).

[31] *GPS Patch Antenna Module Data Sheet*, CDtop Technology (2022), v.05.

[32] F. Stefani, O. Lopez, A. Bercy, W.-K. Lee, C. Chardonnet, G. Santarelli, P.-E. Pottie, and A. Amy-Klein, Tackling the limits of optical fiber links, J. Opt. Soc. Am. B **32**, 787 (2015).

[33] D. Xu, O. Lopez, A. Amy-Klein, and P.-E. Pottie, Non-reciprocity in optical fiber links: Experimental evidence, Opt. Express **29**, 17476 (2021).

[34] NOAA National Centers for Environmental Information (2001): Global Surface Hourly [SYN004BUFR]. NOAA National Centers for Environmental Information (accessed 11-09-2022).

[35] L. C. Sinclair, F. R. Giorgetta, W. C. Swann, E. Baumann, I. Coddington, and N. R. Newbury, Optical phase noise from atmospheric fluctuations and its impact on optical time-frequency transfer, Phys. Rev. A **89**, 023805 (2014).